

Article

Analyzing Power Law Extensions of Newtonian Gravity Using Differential Force Measurements

Thomas Bsaibes  and Ricardo Decca * 

Department of Physics, Indiana University, Indianapolis, IN 46202, USA

* Correspondence: rdecca@iu.edu

Abstract: The Standard Model is not a complete description of reality; it omits the existence of dark matter, dark energy, and an explanation as to why no CP violation has been observed. However, some of these phenomena could be explained through a new force mediated by a new boson. If such a boson were massless it would result in a power law potential and if massive the interaction would be Yukawa-like. A previous experiment employing the interactions of a micromechanical oscillator attached to spherical test mass was successful in placing the best limits on a mass–mass Yukawa-like interaction, but the data were never analyzed in the context of a power law. Here, those data are analyzed considering a power law for powers $n = 1\text{--}5$ where n is the number of boson exchanges. The results show that the limits obtained through power law analysis of these data are not better than the currently accepted limits. A discussion of an experiment design capable of producing better limits on power law extensions to the Standard Model is presented, and suggests that a micromechanical-oscillator-based experiment remains capable of improving the limits by at least one order of magnitude.

Keywords: hypothetical interactions; power-type potentials; constraints on hypothetical particles



Citation: Bsaibes, T.; Decca, R. Analyzing Power Law Extensions of Newtonian Gravity Using Differential Force Measurements. *Metrology* **2024**, *4*, 227–239. <https://doi.org/10.3390/metrology4020014>

Academic Editor: Han Haitjema

Received: 17 February 2024

Revised: 13 April 2024

Accepted: 16 April 2024

Published: 18 April 2024



Copyright: © 2024 by the authors. Licensee MDPI, Basel, Switzerland. This article is an open access article distributed under the terms and conditions of the Creative Commons Attribution (CC BY) license (<https://creativecommons.org/licenses/by/4.0/>).

1. Introduction

The success of the Standard Model (SM) in describing matter and interactions cannot be overstated, but it is not a complete description: it does not explain dark matter and dark energy [1], it predicts charge-parity (CP) violations in the strong force, which have not yet been observed [1–3], and there is no quantized description of gravity [1]. This incompleteness has led to many theories to fill the gaps in the SM.

One such approach is hypothesizing an interaction mediated by an as-yet undiscovered boson [4,5]. If the hypothetical boson is massive it leads to Yukawa-like interactions [6], but if it is massless, the interaction will be parameterized with a power law [7]. This power law is typically written as a correction to Newtonian gravity and for two point masses is expressed as

$$U = \frac{-Gm_1m_2}{r} \left(1 + \Lambda_n \left(\frac{r_0}{r} \right)^{n-1} \right) \quad (1)$$

where G is Newton's gravitational constant, m_1 and m_2 are point masses separated by a distance r , Λ_n is the strength of the correction relative to gravity for a particular power of n , and r_0 is a constant used to preserve the dimension of the interaction; in this work $r_0 = 1 \times 10^{-15}$ m. The value of r_0 was chosen to be the same as in Ref. [8] so that the Λ_n reported in this work can be directly compared to the Λ_n found in Ref. [8].

Previous experiments to probe both power law and Yukawa-like deviations in Newtonian gravity were reported in Refs. [8–10]. One experiment to probe hypothetical Yukawa-like interactions was carried out in 2016 [11]. The Yukawa-like interaction of the form

$$U = \frac{-Gm_1m_2}{r} \left(1 + \alpha e^{r/\lambda} \right) \quad (2)$$

was probed and the experiment placed the best limits on α for a range of $\lambda \in (30, 8000)$ nm, where α is the strength of the correction and λ is the Compton wavelength of a massive hypothetical boson [11]. The experiment consisted of a spherical test mass attached to a micromechanical oscillator that was brought within 200 nm of a source mass made of alternating Au and Si sections, and the force was measured between the two masses. The set-up was not designed to probe power law extensions of the SM and was expected to not be sensitive enough to improve those limits. However, a reanalysis of the force measurements from [11] and a full analysis with the data was never carried out in the context of a power law.

This work carries out a full analysis considering power law extensions of the SM on the force measurements in [11] as well as on new data. The limits obtained are not an improvement over the current best limits [8,10], so we discuss what would need to be done for the approach in [11] to improve limits on power law extensions to the SM.

2. Materials and Methods

Ref. [11] used a differential force measurement technique between a spherical test mass attached to a micromechanical oscillator and a source mass. The test mass was a sphere composed of 3 layers; a central sapphire core with a 149.3 ± 0.2 μm radius covered by 10 nm of Cr followed by 250 nm of Au (see Figure 1 for a cross-sectional diagram of the test and source mass). The sphere was glued to a 500×500 μm micromechanical oscillator and the system had a quality factor $Q \sim 7200$. The deflection of the test mass was measured through a change in capacitance between the oscillator's plate and electrodes located below the plate.

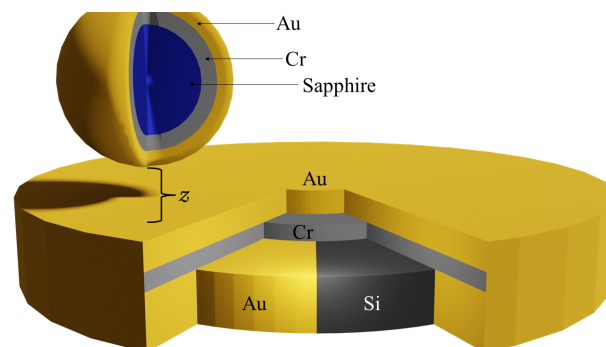


Figure 1. Cut out view (not to scale) of the source mass and test mass showing the individual layers. The source mass has a top Au layer, followed by a Cr layer, and then the alternating Si and Au regions. The test mass has a central sapphire core (shown in blue) coated with Cr and Au. The z indicates the separation and the direction in which the experiment is sensitive.

The source mass was a layered structure consisting of BK7 Schott glass followed by a 2.10 ± 0.02 μm layer of alternating sections of Au and Si. The Au and Si sectors shared a common layer of a 10 ± 1 nm Cr wetting layer, on top of which was a 150 nm Au layer covering the sample. The shared top Au layer thickness was chosen to be larger than the effective penetration depth of the Casimir force. In this way, the contribution due to the Casimir force is the same whether the test mass is located over a Si sector or an Au sector and leads to a Casimir-less measuring technique as described in [12].

The test mass was brought to within 200 nm of the source mass's surface, and at this separation the minimum detectable force is $12 \text{ fN}/\sqrt{\text{Hz}}$. The closest the masses could be brought is ~ 200 nm without the Casimir force making the sphere jump into contact and ruining the whole experiment. The sensitivity also decreases as the separation increases.

The source mass was rotated so that the sections alternated under the test mass at the oscillator's resonant frequency. Doing so makes the experiment select the first harmonic of the force commensurate with the period of the samples.

While the source masses used to set limits on the Yukawa-like interaction [11] had upwards of 300 Au and Si sections, there were source masses that had only two, 1 mm wide, sections of alternating gold and silicon, as depicted in Figure 2. One sample had an inner radius of 2.5 mm and the other had an inner radius of 5 mm. The layered structure is the same as the 300 section samples, except the wetting layer is Ti. The data taken with these larger source masses were not previously analyzed.

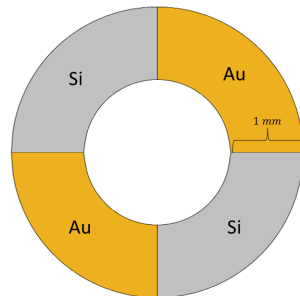


Figure 2. A diagram showing the new source mass geometry, regions alternate between gold and silicon.

To extract limits on Λ_n , the force due to the potential expressed in Equation (1) was calculated by integrating over the experimental geometry. First, the interaction between a spherical test mass and an arbitrary point in the source mass was calculated analytically with a coordinate system centered at the sphere, shown as the unprimed coordinate system in Figure 3, using spherical coordinates (\bar{r}, θ, ϕ) , where θ and ϕ are the polar and azimuthal angle, respectively. The potential energy between the sphere and the source mass is

$$U = -2\pi G\rho_1\rho_2\Lambda_n r_0^{n-1} \iiint \left(\frac{1}{\psi(2-n)} \left[\frac{R(\psi-R)^{3-n}}{3-n} + \frac{(\psi-R)^{4-n}}{(4-n)(3-n)} + \frac{R(\psi+R)^{3-n}}{3-n} - \frac{(\psi+R)^{4-n}}{(4-n)(3-n)} \right] \right) dV_{sm} \quad (3)$$

where R is the radius of the sphere, ρ_1 and ρ_2 are the densities of the sphere and the point, respectively, ψ is the distance from the center of the sphere to the arbitrary point in the source mass, and dV_{sm} is the differential volume of the source mass; see Appendix A for details. It was verified that Equation (3) does not diverge for $n = 2, 3$, and 4 by taking the limit of Equation (3) as $n \rightarrow 2, 3$, and 4 , respectively. These limits can be seen in Appendix A. The integrals over the source mass were carried out using cylindrical coordinates (ϱ, θ', z') in the primed coordinate system, see Figure 3, centered in the middle of the source mass. In the primed coordinate system

$$\psi = \sqrt{\varrho^2 - 2\varrho\varrho_s \cos(\theta' - \theta_s) + \varrho_s^2 + (z' - z_s)^2} \quad (4)$$

where ϱ is the radial variable integrated between the inner and outer radius of the sample, θ' is the angular extent of the sample, ϱ_s is the radial distance to the sphere, θ_s is the angular position of the sphere, z_s is the vertical position of the center of the sphere, and z' is the vertical coordinate integrated over the thickness of the sample.

The experiment is only sensitive to forces in the vertical direction. Normally, calculating the force in the z direction would be carried out by

$$F_z = -\frac{\partial}{\partial z'} U \quad (5)$$

where dF_z is the differential force in the vertical direction that needs to be integrated over the geometry of the source mass. However, since Equation (5) needs to be integrated along z' , calculating the derivative explicitly can be avoided because the operations are the inverse of each other, meaning that the integral of Equation (5) over the source mass in z

is simply the difference of Equation (3) evaluated at the z' integration limits of the source mass, z_1 and z_2 .

$$F_z^{(n)} = \iint (U^{(n)}(z_1) - U^{(n)}(z_2)) dA_{sm} \tag{6}$$

where dA_{sm} is the area element of the source mass that remains to be integrated. A polar coordinate system centered at the center of the sample, the primed coordinate system in Figure 3, is used for the last two integrals. The area element is expressed as $dA_{sm} = \rho d\varrho d\theta'$, where (ϱ, θ') are the polar coordinates in the primed system. The integrals over ϱ and θ' were done numerically with Python code using SciPy version 1.11.4 packages [13].

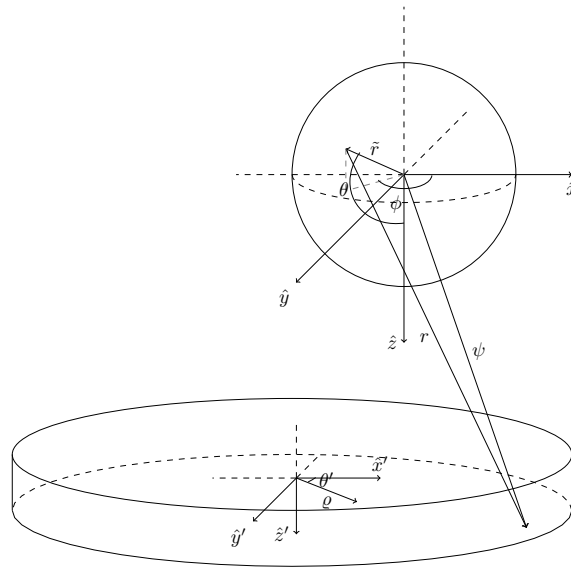


Figure 3. The coordinate system and geometry over which the test mass and source mass were integrated. The unprimed coordinate system is used to integrate over the sphere. θ and ϕ are the polar and azimuthal angle, respectively, ψ is the distance from the center of the sphere to an arbitrary point in the source mass, and r is the separation between points in the sphere and points in the disk. The primed coordinate system is the system used to integrate the geometry of the source mass. θ' is the polar angle in the primed coordinates and ϱ is the radial variable in the source mass system.

In order to obtain the correct interaction from the layered geometry, the numerical integrations were carried out three times, once for each of the three different layers of the test mass. Each test mass layer was considered to be a solid sphere with corresponding radii of $R_{sap} = 149.30 \mu\text{m}$, $R_{Cr} = 149.31 \mu\text{m}$, and $R_{Au} = 149.56 \mu\text{m}$ for sapphire, Cr, and Au, respectively. As an example, for $n = 3$ the integrations for each layer are

$$F_{Au}^{(3)} = 2\pi G r_0^2 \iint \left(\frac{R_{Au}(\psi(z_2) - \psi(z_1))}{\psi(z_1)\psi(z_2)} + \ln \left(\frac{(\psi(z_1) - R_{Au})(\psi(z_2) + R_{Au})}{(\psi(z_1) + R_{Au})(\psi(z_2) - R_{Au})} \right) \right) dA_{sm} \tag{7}$$

$$F_{Cr}^{(3)} = -2\pi G r_0^2 \iint \left(\frac{R_{Cr}(\psi(z_2) - \psi(z_1))}{\psi(z_1)\psi(z_2)} + \ln \left(\frac{(\psi(z_1) - R_{Cr})(\psi(z_2) + R_{Cr})}{(\psi(z_1) + R_{Cr})(\psi(z_2) - R_{Cr})} \right) \right) dA_{sm} \tag{8}$$

$$F_{Sap}^{(3)} = -2\pi G r_0^2 \iint \left(\frac{R_{Sap}(\psi(z_2) - \psi(z_1))}{\psi(z_1)\psi(z_2)} + \ln \left(\frac{(\psi(z_1) - R_{Sap})(\psi(z_2) + R_{Sap})}{(\psi(z_1) + R_{Sap})(\psi(z_2) - R_{Sap})} \right) \right) dA_{sm} \tag{9}$$

Equations (7)–(9) are the integrals over the source mass geometry carried out after the limit of Equation (3) was taken as $n \rightarrow 3$, where $\psi(z_1)$ and $\psi(z_2)$ are Equation (4) evaluated at z_1 and z_2 , respectively. The integrals for the other powers were carried out in the same manner. Once the integrals for each test mass layer are carried out, the total force due to the layered structure of the source mass and test mass (Figure 1) is

$$F_z^{(3)} = \Lambda_3(\rho_{Au} - \rho_{Si})((\rho_{Sap} - \rho_{Cr})F_{Sap}^{(3)} + (\rho_{Cr} - \rho_{Au})F_{Cr}^{(3)} + \rho_{Au}F_{Au}^{(3)}) \tag{10}$$

where ρ_{Au} , ρ_{Cr} , ρ_{sap} , and ρ_{Si} are the densities of Au, Cr, sapphire, and Si, respectively, $F_z^{(3)}$ indicates the total force in the z-direction for the power $n = 3$, and the factor out front, $(\rho_{Au} - \rho_{Si})$, accounts for the difference when the sphere is over an Au or Si sector in the source mass. Furthermore, since the first two layers are a shared layer of Au and Cr, the contributions of these layers to the interaction are subtracted out.

The total force was calculated with the test mass at different angular positions (θ'_s), Figure 4. The amplitude of the first harmonic for a particular power, $A_1^{(n)}$, of the force commensurate with the period, Θ , of the sectors was equated to the error bars of the force measurements,

$$A_1^{(n)} = \frac{2}{\Theta} \int_0^{\Theta} F_z^{(n)} \cos\left(\frac{2\pi\theta_s}{\Theta}\right) d\theta_s. \tag{11}$$

The error bar value is $f_{err} = 0.13$ fN at a separation of 300 nm, as shown in Figure 5. Equating the calculated first harmonic of the force to the experimental error bar allows limits on Λ_n to be extracted,

$$\Lambda_n = \frac{f_{err}}{A_1^{(n)}}. \tag{12}$$

The same method to determine limits was used for the powers of $n = 1$ to 5. Table 1 shows the limits placed on Λ_n from both the 300 sector source masses used in [11] and the 4 sector source mass with inner radius of 2.5 mm as depicted in Figure 2.

Table 1. The constraints placed on Λ_n from our experiment compared to the limits reported in [8]. The two rightmost columns are the limits calculated using the data from the many-sector samples and the large-sector samples.

| n | Λ_n from [8] | Λ_n Many-Sector Sample | Λ_n Large-Sector Sample |
|-----|----------------------|--------------------------------|---------------------------------|
| 1 | 1×10^{-9} | 8.0×10^8 | 3.0×10^2 |
| 2 | 3.7×10^8 | 6.1×10^{15} | 2.5×10^{13} |
| 3 | 7.5×10^{19} | 7.9×10^{24} | 8.8×10^{23} |
| 4 | 2.2×10^{31} | 1.2×10^{34} | 5.2×10^{33} |
| 5 | 6.7×10^{42} | 1.4×10^{43} | 1.0×10^{43} |

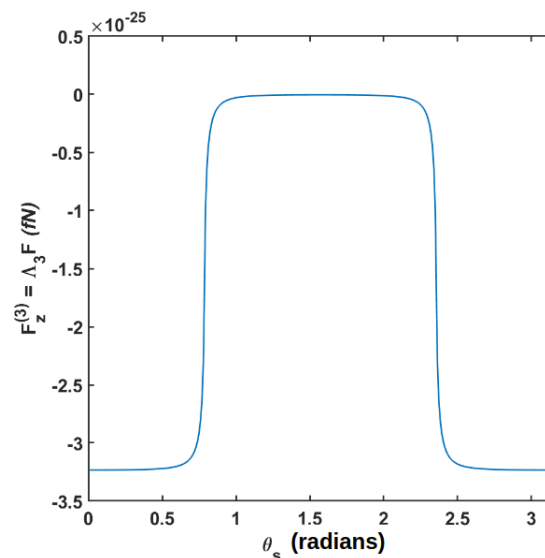


Figure 4. The total force as the angular location of the sphere changes, which is equivalent to fixing the location of the sphere and rotating the sample. The first harmonic of the force in accordance with the period of the sectors is calculated and equated to the error bars of the force measurement to extract Λ_n . This example is from Equation (10), where $F = \frac{F_z^3}{\Lambda_3^3}$, F_z^3 from Equation (10).

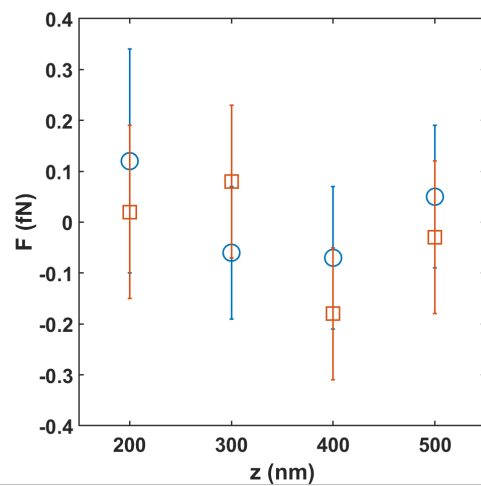


Figure 5. Measured force as a function of separation of the large source mass. The blue circle data correspond to the sample with an inner radius of 2.5 mm and the orange squares are the data from the 5 mm inner radius sample.

3. Results

The limits presented in Table 1 were calculated using results from an experiment that was not designed to probe power law extensions to the SM. The best limit on Λ_n with this geometry came from the large-sector sample, but these limits are not better than the ones found in Ref. [8].

The reported values of Λ_n in this work are large because those are the best limits that can be placed given these experimental data. As an example, for $n = 5$, we are not claiming the value of $\Lambda_5 = 10^{43}$, rather we assert that Λ_5 would need to be of that order for this experiment to have seen its effects, and likewise for the other values of n considered in this work. These are the values for Λ_n that, for the used geometry, provide an interaction equal to our sensitivity.

4. Discussion

While the experiment did not yield better limits on Λ_n , changes could be made that would improve the system’s sensitivity. For example, if the source masses were designed with a power law in mind, the limits could be further improved. Figure 6 shows the potential limits for Λ_5 as a function of the sample’s radial extent (ϱ) for a thickness of 2 mm. The limits have a similar functional dependence with the other dimensions of the sample as the radius increases. The improvement is attributed to the larger volume of interaction improving the sensitivity of the measurement, yielding better limits. However, the improvement gained in the limits by increasing the source mass’s volume quickly diminishes.

Altering the test mass to also have a larger volume of interaction could provide a small improvement on power law limits. Considering a system, like the one proposed in [14], where the test mass is cylindrical. If the spherical test mass is exchanged for a cylindrical one, and we carry out a similar analysis of the one described above, the expected limits using the new test mass can be calculated. The details of the calculation can be found in Appendix B. The following is the expression of the force between a cylindrical test mass and an infinite slab with thickness $t = 2$ mm along the vertical direction

$$F_5 = \frac{-\pi^2 G \rho_1 \rho_2 L \Lambda_5 r_0^4}{3} \left(\frac{A_2^2}{(R^2 - A_2^2) \sqrt{A_2^2 - R^2}} - \frac{A_1^2}{(R^2 - A_1^2) \sqrt{A_1^2 - R^2}} \right) \tag{13}$$

where $A_1 = d + R_{Au}$, $A_2 = A_1 + t$, and $L = 500 \mu\text{m}$ the length of the cylinder. The expected limits for the powers $n \in [1, 5]$ using a cylindrical test mass are listed in Table 2,

calculated using a separation $d = 200$ nm. Only the power $n = 5$ is expected to improve by about an order of magnitude using a cylinder. Using a cylinder with a length of $500 \mu\text{m}$ and radius of curvature $R = 150 \mu\text{m}$ optimizes the sensitivity given the constraints of the micromechanical oscillator and the lithographic fabrication method of the cylinder.

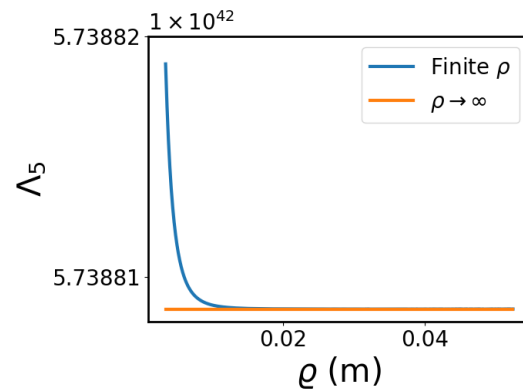


Figure 6. The limits on Λ_5 can be marginally improved if the size of the source mass is designed with power law interactions in mind. Shown here are the estimated limits for $n = 5$ as a function of the width of the source mass. However, the improvement gained by increasing the source mass size quickly diminishes. The constant orange line is the limit that would be achieved as the width of the source mass goes to infinity.

Table 2. The constraints that could be placed on Λ_n if a cylindrical test mass were used with a source mass designed to probe power law potentials.

| n | Λ_n from [8] | Cylindrical Test Mass |
|-----|----------------------|-----------------------|
| 1 | 1×10^{-9} | 6.1×10^{-2} |
| 2 | 3.7×10^8 | 4.4×10^{10} |
| 3 | 7.5×10^{19} | 2.0×10^{22} |
| 4 | 2.2×10^{31} | 1.1×10^{32} |
| 5 | 6.7×10^{42} | 2.8×10^{41} |

Other aspects of the experimental design could be change but would either have little impact or have fabrication limitations. One could conceivably use source mass materials that have larger difference in density since, as seen in Equation (10), the response is proportional to the difference in densities between the two materials. Changing the source materials, however, will not improve the signal by more than a factor of ~ 2 if using Osmium and air. Certainly, our selection of Au and Si is not optimal, but as they are relatively easy to work with, we think it is a convenient selection. In regards to the test mass, Au is again a suitable choice. A thicker layer of Au would benefit the experiment; however, we started to observe a peel off of the Au from the sphere at 300 nm.

5. Conclusions

Improving the limits of power law extensions to gravity is a challenging endeavor, and new methods are needed to continue to make improvements on short-range interaction experiments. While these types of mechanical measurements have a high precision even at separations of ~ 200 nm, this work shows that the size of the masses limit the sensitivity when probing power law interactions. The limit on Λ_5 , reported here to be 1.0×10^{43} , is expected to improve about an order of magnitude the best current limits [8] if a cylindrical test mass were used. The cylinder has a larger interaction volume when compared to a sphere, which results in a higher sensitivity. Several experimental approaches are being developed to test gravity at short distances, seeking signs of deviations potentially due to dark matter effects [15–22]. The description of these new approaches does not explicitly state probing power law extensions to the SM. Researchers should evaluate whether

these new techniques are equally suited to test power law models as well as Yukawa-like interactions, which could result in a larger selection of theories being ruled out.

Author Contributions: Conceptualization, T.B. and R.D.; methodology, T.B. and R.D.; validation, T.B. and R.D.; formal analysis, T.B.; investigation, T.B.; data curation, T.B.; writing—original draft preparation, T.B.; writing—review and editing, T.B. and R.D.; visualization, T.B.; supervision, R.D. All authors have read and agreed to the published version of the manuscript.

Funding: This research received no external funding.

Data Availability Statement: All data is available upon request.

Conflicts of Interest: The authors declare no conflicts of interest.

Appendix A. Detailed Calculation Method for Sphere Test Mass Geometry

$$dU = -G\rho_{tm}\rho_{sm}\Lambda_n r_0^{n-1} \left(\frac{dV_{tm}dV_{sm}}{r^n} \right) \tag{A1}$$

Equation (A1) is the differential potential that needs to be integrated to calculate the interaction between the test mass and the source mass, where G is Newton’s gravitational constant, ρ_{tm} (ρ_{sm}) is the density of the test mass (source mass), Λ_n is the strength of the correction for a particular power n , r_0 is a constant used to preserve the dimension, dV_{tm} (dV_{sm}) is the test mass (source mass) volume element, and r is the distance between a point in the test mass and a point in the source mass and is expressed as

$$r = \sqrt{\tilde{r}^2 + \psi^2 - 2\tilde{r}\psi \cos(\theta)}. \tag{A2}$$

where \tilde{r} is the radial coordinate of a point in the sphere and has integration limits from zero to the radius of the sphere, θ is the polar coordinate of the sphere, and ψ is the distance from the center of the spherical test mass to an arbitrary point in the source mass. We use spherical coordinates to integrate the test mass, so the test mass volume element is expressed as

$$dV_{tm} = \tilde{r}^2 d\tilde{r} d(\cos(\theta)) d\phi. \tag{A3}$$

The integral over the test mass is carried out as follows

$$dU = -G\rho_{tm}\rho_{sm}\Lambda_n r_0^{n-1} \left(\int_0^R \int_{-1}^1 \int_0^{2\pi} \frac{\tilde{r}^2 d\tilde{r} d(\cos(\theta)) d\phi}{(\tilde{r}^2 + \psi^2 - 2\tilde{r}\psi \cos(\theta))^{n/2}} \right) dV_{sm}. \tag{A4}$$

Nothing in Equation (A4) depends on azimuthal angle, ϕ , so the integral over ϕ results in a factor of 2π .

$$dU = -2\pi G\rho_{tm}\rho_{sm}\Lambda_n r_0^{n-1} \left(\int_0^R \int_{-1}^1 \frac{\tilde{r}^2 d\tilde{r} d(\cos(\theta))}{(\tilde{r}^2 + \psi^2 - 2\tilde{r}\psi \cos(\theta))^{n/2}} \right) dV_{sm} \tag{A5}$$

Using the following change of variables: $x = \cos(\theta)$ and $u^2 = \tilde{r}^2 - 2\tilde{r}\psi x + \psi^2$, Equation (A5) is now

$$dU = -2\pi G\rho_{tm}\rho_{sm}\Lambda_n r_0^{n-1} \left(\int_0^R \int_{(\psi+\tilde{r})}^{(\psi-\tilde{r})} \frac{\tilde{r} u^{1-n} du d\tilde{r}}{\psi} \right) dV_{sm} \tag{A6}$$

and carrying out the last two integrals for the test mass, we are left with the potential between the sphere and an arbitrary point in the source mass.

$$dU = \frac{-2\pi G\rho_{tm}\rho_{sm}\Lambda_n r_0^{n-1}}{\psi(2-n)(3-n)(4-n)} \left(R(4-n)(\psi-R)^{3-n} + (\psi-R)^{4-n} + R(4-n)(\psi+R)^{3-n} - (\psi+R)^{4-n} \right) dV_{sm} \tag{A7}$$

For $n = 2, 3,$ and $4,$ Equation (A7) yields $0/0;$ as such, it needs to be verified that it does not diverge by taking the limits as $n \rightarrow 2, 3,$ and $4.$ Taking the limit of Equation (A7)

$$\lim_{n \rightarrow 2,3,\text{or }4} \frac{(R(4-n)(\psi-R)^{3-n} + (\psi-R)^{4-n} + R(4-n)(\psi+R)^{3-n} - (\psi+R)^{4-n})}{(2-n)(3-n)(4-n)} \tag{A8}$$

and using l'Hôpital's rule to evaluate (A8) results in

$$\lim_{n \rightarrow 2,3,\text{or }4} \left[\frac{(R((\psi-R)^{3-n}(n-4)\ln(\psi-R) - (\psi-R)^{3-n}) - (\psi-R)^{4-n}\ln(\psi-R))}{-((3-n)(4-n) + (2-n)(4-n) + (2-n)(3-n))} + \frac{R((\psi+R)^{3-n}(n-4)\ln(\psi+R) - (\psi+R)^{3-n}) + (\psi+R)^{4-n}\ln(\psi+R)}{-((3-n)(4-n) + (2-n)(4-n) + (2-n)(3-n))} \right] \tag{A9}$$

Evaluating Equation (A9) for $n = 2, 3,$ or 4 shows that (A7) does not diverge, see Table A1.

Table A1. The results of taking the limit of Equation (A9) for powers $n = 2, 3,$ and 4 showing that Equation (A7) does not diverge for those powers.

| n | Limit Result |
|-----|---|
| 2 | $R\psi + \frac{(\psi^2-R^2)}{2} \ln\left(\frac{\psi-R}{\psi+R}\right)$ |
| 3 | $-2R - \psi \ln\left(\frac{\psi-R}{\psi+R}\right)$ |
| 4 | $\frac{\psi R}{\psi^2-R^2} - \frac{1}{2} \ln\left(\frac{\psi-R}{\psi+R}\right)$ |

It was verified that integrating (A6) the powers $n = 2, 3,$ and 4 yield the same expressions as taking the limit expressed in Equation (A9). Now that it is shown that Equation (A7) does not diverge, all that is left is to integrate over the source mass.

Appendix B. Detailed Calculation Method for Cylinder Test Mass Geometry

The starting point to calculate the interaction between an infinite slab and a cylinder is the potential

$$dU = -G\rho_{sm}\Lambda_n r_0^{n-1} \left(\frac{dV_{sm}}{r^n}\right). \tag{A10}$$

The procedure to integrate the cylinder-slab geometry is the following

1. Integrate over the source mass;
2. Calculate the field due to the source mass, $\vec{g},$ along $\hat{z};$
3. Calculate the force, $F_z^{(n)} = \vec{g}m_{tm},$ where m_{tm} is the mass of the test mass calculated using $m_{tm} = \iiint \rho_{tm}dV_{tm},$ where ρ_{tm} is the density of the test mass and $dV_{tm} = dx dy dz$ is the volume element of the test mass.

The coordinate system used for integrating the infinite slab-cylinder geometry is shown in Figure A1.

First, we will start with the integral over the source mass.

$$dU = -G\rho_{sm}\Lambda_n r_0^{n-1} \iiint \frac{dV_{sm}}{r^n} \tag{A11}$$

$$= -G\rho_{sm}\Lambda_n r_0^{n-1} \iiint \frac{\rho d\rho d\theta dz}{(\rho^2 + (z' - z)^2)^{n/2}} \tag{A12}$$

The limits of integration over the source mass are $\rho \in [0, \infty), \theta \in [0, 2\pi], z \in [0, -t].$ Integrating over θ and carrying out the change of variable $s^2 = \rho^2 + (z' - z)^2$

$$U = -2\pi G\rho_{sm}\Lambda_n r_0^{n-1} \int_{z'-z}^{\infty} \frac{ds}{s^{n-1}} \tag{A13}$$

$$= -2\pi G\rho_{sm}\Lambda_n r_0^{n-1} \int_0^{-t} \frac{dz}{(2-n)(z'-z)^{n-2}} \tag{A14}$$

$$= \frac{-2\pi G\rho_{sm}\Lambda_n r_0^{n-1}}{(2-n)(3-n)} (z'^{3-n} - (z'+t)^{3-n}) \tag{A15}$$

Equation (A15) is used for $n = 1, 4,$ and 5 ; for $n = 2$ and 3 , Equation (A10) was integrated specifically for those powers.

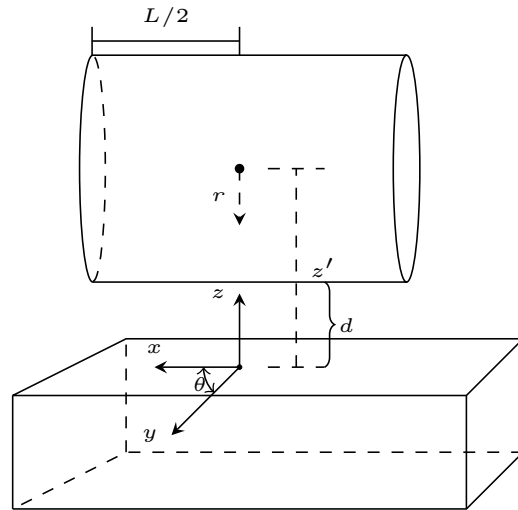


Figure A1. The coordinate system used to integrate over the infinite slab–cylinder geometry. L is the length of the cylinder and d is the distance from the top of the slab to the bottom of the cylinder.

The field is along \hat{z} due to the source mass is calculated by

$$\vec{g} = -\frac{dU}{dz'}\hat{z} \tag{A16}$$

Appendix B.1. $n = 1$

$$U = \frac{-2\pi G\rho_{sm}\Lambda_1}{(2-1)(3-1)} (z'^{3-1} - (z'+t)^{3-1}) \tag{A17}$$

$$\vec{g} = -2\pi G\rho_{sm}\Lambda_1 t\hat{z} \tag{A18}$$

$$F_z^{(1)} = \vec{g}m_{tm} = -2\pi G\rho_{sm}\Lambda_1 t\hat{z}(\rho_{tm}\pi R^2 L) \tag{A19}$$

Appendix B.2. $n = 2$

$$dU = -G\rho_{sm}\Lambda_2 r_0 \iiint \frac{dV_{sm}}{r^2} \tag{A20}$$

$$= -G\rho_{sm}\Lambda_2 r_0 \iiint \frac{\rho d\rho d\theta dz}{\rho^2 + (z'-z)^2} \tag{A21}$$

Here, the limits of integration for ρ are $\rho \in [0, \rho_+]$. Integrating with respect to θ and making the following substitution $s = \rho^2 + (z'-z)^2$ gives

$$dU = -\pi G\rho_{sm}\Lambda_2 r_0 \int_{(z'-z)^2}^{\rho_+^2 + (z'-z)^2} \frac{ds}{s} \tag{A22}$$

$$U = -\pi G\rho_{sm}\Lambda_2 r_0 \int_0^{-t} \ln\left(\frac{\rho_+^2 + (z'-z)^2}{(z'-z)^2}\right) dz \tag{A23}$$

$$\vec{g} = -\frac{dU}{dz}\hat{z} = \pi G\rho_{sm}\Lambda_2 r_0 \frac{d}{dz} \int_0^{-t} \ln\left(\frac{\rho_+^2 + (z' - z)^2}{(z' - z)^2}\right) dz \tag{A24}$$

$$= \pi G\rho_{sm}\Lambda_2 r_0 \left(\ln\left(\frac{\rho_+^2 + (z' + t)^2}{(z' + t)^2}\right) - \ln\left(\frac{\rho_+^2 + z'^2}{z'^2}\right) \right) \tag{A25}$$

$$= \pi G\rho_{sm}\Lambda_2 r_0 \left(\ln\left(\frac{\rho_+^2 + (z' + t)^2}{\rho_+^2 + z'^2}\right) - \ln\left(\frac{(z' + t)^2}{z'^2}\right) \right) \tag{A26}$$

Since we are considering the source mass as an infinite slab, we take $\rho_+ \rightarrow +\infty$

$$\lim_{\rho_+ \rightarrow +\infty} \ln\left(\frac{\rho_+^2 + (z' + t)^2}{\rho_+^2 + z'^2}\right) = 0 \tag{A27}$$

$$\vec{g} = -\pi G\rho_{sm}\Lambda_2 r_0 \ln\left(\frac{(z' + t)^2}{z'^2}\right) \tag{A28}$$

$$F_z^{(2)} = \iiint \vec{g}(z')\rho_{tm} dx dy dz' \tag{A29}$$

$$F_z^{(2)} = -\pi G\rho_{sm}\rho_{tm}\Lambda_2 r_0 \iiint \ln\left(\frac{(z' + t)^2}{z'^2}\right) dx dy dz' \tag{A30}$$

The limits of integration over the cylindrical test mass are $x \in [-L/2, L/2]$, $y \in [0, \sqrt{R^2 - r^2}]$, and $r \in [-R, R]$ with $r = d + R - z'$ and $dr = -dz'$

$$F_z^{(2)} = -\pi G\rho_{sm}\rho_{tm}\Lambda_2 r_0 L \int_{-R}^R \int_0^{\sqrt{R^2 - r^2}} \ln\left(\frac{(d + R + t - r)^2}{(d + R - r)^2}\right) dy (-dr) \tag{A31}$$

$$= -\pi G\rho_{sm}\rho_{tm}\Lambda_2 r_0 L \int_{-R}^R \sqrt{R^2 - r^2} \ln\left(\frac{(d + R + t - r)^2}{(d + R - r)^2}\right) (-dr) \tag{A32}$$

We could not find an analytical solution to the final integral, and it was solved numerically.

Appendix B.3. $n = 3$

$$dU = -G\rho_{sm}\Lambda_3 r_0^2 \iiint \frac{\rho d\rho d\theta dz}{(\rho^2 + (z' - z)^2)^{3/2}} \tag{A33}$$

Integrating θ and substituting $s^2 = (\rho^2 + (z' - z)^2)^{1/2}$

$$U = -2\pi G\rho_{sm}\Lambda_3 r_0^2 \int_0^{-t} \int_{z'-z}^{\infty} \frac{ds dz}{s^2} \tag{A34}$$

$$= -2\pi G\rho_{sm}\Lambda_3 r_0^2 \int_0^{-t} \frac{dz}{2(z' - z)} \tag{A35}$$

$$= \pi G\rho_{sm}\Lambda_3 r_0^2 \ln\left(\frac{z' + t}{z'}\right) \tag{A36}$$

$$\vec{g} = -\pi G\rho_{sm}\Lambda_3 r_0^2 \left(\frac{1}{z' + t} - \frac{1}{z'} \right) \tag{A37}$$

$$F_z^{(3)} = -\pi G \rho_{sm} \rho_{tm} \Lambda_3 r_0^2 \iiint \left(\frac{1}{z'+t} - \frac{1}{z'} \right) dx dy dz' \tag{A38}$$

$$F_z^{(3)} = -\pi G \rho_{sm} \rho_{tm} \Lambda_3 r_0^2 L \int_{-R}^R \int_0^{\sqrt{R^2-r^2}} \left(\frac{-dy dr}{d+R+t-r} + \frac{dy dr}{d+R-r} \right) \tag{A39}$$

$$F_z^{(3)} = -\pi G \rho_{sm} \rho_{tm} \Lambda_3 r_0^2 L \int_{-R}^R \left(\frac{-\sqrt{R^2-r^2}}{d+R+t-r} + \frac{\sqrt{R^2-r^2}}{d+R-r} \right) dr \tag{A40}$$

$$F_z^{(3)} = -\pi G \rho_{sm} \rho_{tm} \Lambda_3 r_0^2 L \left(\frac{-\pi(d+R+t)^2}{2((d+R+t)^2 - R^2)^{3/2}} + \frac{\pi(d+R)^2}{2((d+R)^2 - R^2)^{3/2}} \right) \tag{A41}$$

Appendix B.4. $n = 4$

Starting with Equation (A15) for $n = 4$

$$U = \frac{-2\pi G \rho_{sm} \Lambda_4 r_0^3}{2} \left(\frac{1}{z'} - \frac{1}{z'+t} \right) \tag{A42}$$

$$\vec{g} = \pi G \rho_{sm} \Lambda_4 r_0^3 (-z'^{-2} + (z'+t)^{-2}) \tag{A43}$$

$$F_z^{(4)} = -\pi G \rho_{sm} \Lambda_4 r_0^3 \iiint (z'^{-2} - (z'+t)^{-2}) dx dy dz' \tag{A44}$$

$$F_z^{(4)} = -\pi G \rho_{sm} \Lambda_4 r_0^3 L \int_0^{\sqrt{R^2-r^2}} \int_{-R}^R (z'^{-2} - (z'+t)^{-2}) dy (-dr) \tag{A45}$$

$$F_z^{(4)} = -\pi G \rho_{sm} \rho_{tm} \Lambda_4 r_0^3 L \left(\frac{A_2 \pi}{\sqrt{A_2^2 - R^2}} - \frac{A_1 \pi}{\sqrt{A_1^2 - R^2}} \right) \tag{A46}$$

$$A_2 = d + R + t \text{ and } A_1 = d + R$$

Appendix B.5. $n = 5$

Starting with Equation (A15) for $n = 5$

$$U = \frac{-\pi G \rho_{sm} \Lambda_5 r_0^4}{3} \left(\frac{1}{z'^2} - \frac{1}{(z'+t)^2} \right) \tag{A47}$$

$$\vec{g} = \frac{-2\pi G \rho_{sm} \Lambda_5 r_0^4}{3} \left(\frac{1}{z'^3} - \frac{1}{(z'+t)^3} \right) \tag{A48}$$

$$F_z^{(5)} = \frac{-2\pi G \rho_{sm} \Lambda_5 r_0^4}{3} \iiint \left(\frac{1}{z'^3} - \frac{1}{(z'+t)^3} \right) dx dy dz' \tag{A49}$$

$$x \in [-L/2, L/2], y \in [0, \sqrt{R^2-r^2}], r = d + R - z', dr = -dz'$$

$$F_z^{(5)} = \frac{-\pi G \rho_{sm} \Lambda_5 r_0^4 L}{3} \left(\frac{A_1^2}{(A_1^2 - R^2)^{3/2}} - \frac{A_2^2}{(A_2^2 - R^2)^{3/2}} \right) \tag{A50}$$

$$A_2 = d + R + t \text{ and } A_1 = d + R$$

References

1. Langacker, P. *The Standard Model and Beyond*; Taylor & Francis: Abingdon, UK, 2017.
2. Kiefer, C. *Why Quantum Gravity?* Springer: Berlin/Heidelberg, Germany, 2007.
3. Rovelli, C. *Quantum Gravity*; Cambridge University Press: Cambridge, UK, 2004.
4. Weinberg, S. A new light boson? *Phys. Rev. Lett.* **1978**, *40*, 223. [[CrossRef](#)]
5. Klimchitskaya, G.L.; Mostepanenko, V.M. Dark Matter Axions, Non-Newtonian Gravity and Constraints on Them from Recent Measurements of the Casimir Force in the Micrometer Separation Range. *Universe* **2021**, *7*, 343. [[CrossRef](#)]

6. Banks, H.; McCullough, M. Charting the fifth force landscape. *Phys. Rev. D* **2021**, *103*, 075018. [[CrossRef](#)]
7. Adelberger, E.; Heckel, B.R.; Hoedl, S.; Hoyle, C.; Kapner, D.; Upadhye, A. Particle-physics implications of a recent test of the gravitational inverse-square law. *Phys. Rev. Lett.* **2007**, *98*, 131104. [[CrossRef](#)] [[PubMed](#)]
8. Klimchitskaya, G.L. Constraints on Theoretical Predictions beyond the Standard Model from the Casimir Effect and Some Other Tabletop Physics. *Universe* **2021**, *7*, 47. [[CrossRef](#)]
9. Adelberger, E.; Heckel, B.; Nelson, A. Tests of The Gravitational Inverse-Square Law. *Annu. Rev. Nucl. Part. Sci.* **2003**, *53*, 77–121. [[CrossRef](#)]
10. Tan, W.H.; Du, A.B.; Dong, W.C.; Yang, S.Q.; Shao, C.G.; Guan, S.G.; Wang, Q.L.; Zhan, B.F.; Luo, P.S.; Tu, L.C.; et al. Improvement for testing the gravitational inverse-square law at the submillimeter range. *Phys. Rev. Lett.* **2020**, *124*, 051301. [[CrossRef](#)] [[PubMed](#)]
11. Chen, Y.J.; Tham, W.K.; Krause, D.E.; López, D.; Fischbach, E.; Decca, R.S. Stronger Limits on Hypothetical Yukawa Interactions in the 30–8000 nm Range. *Phys. Rev. Lett.* **2016**, *116*, 221102. [[CrossRef](#)] [[PubMed](#)]
12. Decca, R.; Lopez, D.; Chan, H.; Fischbach, E.; Krause, D.; Jamell, C. Constraining new forces in the Casimir regime using the isoelectronic technique. *Phys. Rev. Lett.* **2005**, *94*, 240401. [[CrossRef](#)]
13. Virtanen, P.; Gommers, R.; Oliphant, T.E.; Haberland, M.; Reddy, T.; Cournapeau, D.; Burovski, E.; Peterson, P.; Weckesser, W.; Bright, J.; et al. SciPy 1.0: Fundamental Algorithms for Scientific Computing in Python. *Nat. Methods* **2020**, *17*, 261–272. [[CrossRef](#)] [[PubMed](#)]
14. Bsaibes, T.; Pires, L.; Czaplewski, D.; López, D.; Decca, R.S. Toward a better system for short range precision force measurements. *Mod. Phys. Lett. A* **2020**, *35*, 2040002. [[CrossRef](#)]
15. Timberlake, C.; Vinante, A.; Shankar, F.; Lapi, A.; Ulbricht, H. Probing modified gravity with magnetically levitated resonators. *Phys. Rev. D* **2021**, *104*, L101101. [[CrossRef](#)]
16. Westphal, T.; Hepach, H.; Pfaff, J.; Aspelmeyer, M. Measurement of gravitational coupling between millimetre-sized masses. *Nature* **2021**, *591*, 225–228. [[CrossRef](#)] [[PubMed](#)]
17. Sedmik, R.I.P.; Pitschmann, M. Next Generation Design and Prospects for Cannex. *Universe* **2021**, *7*, 234. [[CrossRef](#)]
18. Barker, P.F.; Bose, S.; Marshman, R.J.; Mazumdar, A. Entanglement based tomography to probe new macroscopic forces. *Phys. Rev. D* **2022**, *106*, L041901. [[CrossRef](#)]
19. Shi, H.; Zhuang, Q. Ultimate precision limit of noise sensing and dark matter search. *npj Quantum Inf.* **2023**, *9*, 27. [[CrossRef](#)]
20. Moore, D.C.; Geraci, A.A. Searching for new physics using optically levitated sensors. *Quantum Sci. Technol.* **2021**, *6*, 014008. [[CrossRef](#)]
21. Kawasaki, A. Measurement of the Newtonian constant of gravitation G by precision displacement sensors. *Class. Quantum Gravity* **2020**, *37*, 075002. [[CrossRef](#)]
22. Tino, G.M. Testing gravity with cold atom interferometry: Results and prospects. *Quantum Sci. Technol.* **2021**, *6*, 024014. [[CrossRef](#)]

Disclaimer/Publisher’s Note: The statements, opinions and data contained in all publications are solely those of the individual author(s) and contributor(s) and not of MDPI and/or the editor(s). MDPI and/or the editor(s) disclaim responsibility for any injury to people or property resulting from any ideas, methods, instructions or products referred to in the content.